Electronic Supplementary Information

Tin Chalcohalide $Sn_{11}(PS_4)_4I_{10}$ Obtained by Structural-template-oriented Synthesis: Exhibiting Balanced Infrared Nonlinear Optical Performance

Deng Cuier [a,b#], Xi Xu [a#], Yuhan Hua [a,b], Jingyu Guo[a,b*], Li-Ming Wu[a,b*] and Ling Chen[a,b*]

[a]Faculty of Arts and Sciences, Beijing Normal University, Zhuhai 519087, Peoples R China

[b]Beijing Key Laboratory of Energy Conversion and Storage Materials, College of Chemistry, Beijing Normal University, Beijing, 100875, Peoples R China

[#] These authors contributed equally to this work.

* Corresponding author: chenl@bnu.edu.cn, wlm@bnu.edu.cn and jyguo@bnu.edu.cn

Table of Contents

Experimental Procedures

Single crystal X-ray diffraction and Powder XRD Analysis. A Bruker SMART APEX IV 4K CCD diffractometer with Mo *Kα* radiation (λ = 0.71073 Å) was used to collect the single-crystal X-ray diffraction (XRD) data at 296(2) K, and the data were integrated through a SAINT program[1]. The direct methods and SHELXTL system[2] were used to solve and refine the crystal structure, respectively. The powder X-ray diffraction (XRD) was performed on Bruker D2 PHASER diffractometer equipped with Cu *Kα* radiation at room temperature, which diffraction patterns were recorded with the 2θ range from 10 to 70°, the scanning step width was 0.02° and the scanning rate was 1 s/step.

UV Diffuse-reflectance Spectroscopy. The UV-Vis-NIR diffuse reflectance spectrum for SPSI was characterized by a Shimadzu UV-3600i Plus UV-Vis-NIR spectrophotometer to determine the accurate absorption edge of the compound at room temperature within the wavelength range from 180 to 1700 nm. And the reflectance spectrum was transformed to absorbance using the Kubelka-Munk function[3].

Infrared (IR) spectroscopy. Infrared (IR) spectra was recorded on a Thermo Scientific Nicolet iS50 FT-IR spectrophotometer in the range from 400 to 4000 cm^{-1} with a resolution of 1 cm^{-1}. The sample was mixed thoroughly with 500 mg of dried KBr.

SHG Measurement. SHG responses in this work were measured according to the modified Kurtz Perry method[4]. Powder samples and commercial AGS crystals were separately crushed and sieved into five particle size ranges: 30-45, 45-75, 75-109, 109-150, and 150-212 μm. These samples were filled in a silicone gasket and held between two glass slices. A 2100 nm pulse (1 Hz, 10 ns) laser was used for SHG measurements. SHG signals were collected by a detector, observed, and recorded by an oscilloscope.

Birefringence Measurement. The refractive index difference of SPSI was characterized by using the polarizing microscope equipped (ZEISS Axis Scope. 5 pol) with Berek compensator[5]. The average wavelength of the light source was 546 nm. The formula for calculating the birefringence is listed below, $R = | N_g - N_p | \times d = \Delta n \times d$ (1)

Here, R represents the optical path difference; N_g, N_p and Δn means the refractive index of fast light, slow light, and the difference value of refractive index, respectively; d denotes the thickness of the crystal.

LIDT Measurement. LIDT measurements of powder samples and commercial AGS crystals (powder samples with particle size range of 150–212 μm) were measured with a 1064 nm pulse laser (pulse width: 10 ns) applied. Laser energy increased from 0.1 mJ continually until the damage spots were observed through a microscope. The formula for calculating LIDT is listed below,

LIDT = Damage energy/(Damage area × Pulse width) (2)

Thermal Analysis. A NETZSCH STA 449C instrument was used to examine the thermal stability of SPSI under static N_2 conditions. The sample and reference (Al_2O_3) were encapsulated in

a Pt crucible, which was heated up to 800 ℃ at a rate of 10 ℃/min, and then cooled to room temperature.

Theoretical calculations. First principles calculations on electronic structures and linear optical properties were carried out by the Vienna Ab initio Simulation Package (VASP)[6,7]. The projector augmented wave[8] (PAW) method was used to treat valence-core interactions. The 5*s* and 5*p* states of Sn atoms, the 3*s* and 3*p* states of P atoms, the 3*s* and 3*p* states of S atoms and the 5*s* and 5*p* states of I atoms were treated as valance states. The energy cutoff of the plane wave basis was set to be 400 eV. The convergence criterion for self-consistent iterations was set to be 10^{-6} eV. The Brillouin zone was sampled by a Γ-centerd 4×4×3 mesh. For the structural relaxation, we used the Perdew-Burke-Ernzerhof (PBE) functional as the exchange-correlation potential. The residual forces on atoms were less than 0.005 eV/Å. Because of the well-known underestimation of band gaps with semilocal functionals, we turn to the screened hybrid functional Heyd-Scuseria-Ernzerhof (HSE06) for further calculations of band structures and linear optical properties after structural relaxation. The frequency-dependent dielectric matrix was calculated with the summation-over-states approach[9], and then linear optical properties, including the refractive index n and the birefringence Δn, can be obtained accordingly. For non-linear optical properties, we take advantage of the ABINIT package[10] and the nonlinear optical coefficients were calculated with the density functional perturbation theory[11].

Table S1. Crystal data and structure refinement for $Sn_{11}(PS_4)_4I_{10}$

Empirical formula	$Sn_{11}(PS_4)_4I_{10}$
Formula weight	3211.43
Temperature (K)	302
Wavelength (Å)	0.71073
Crystal system	Tetragonal
Space group	$I\bar{4}2m$
Unit cell dimensions	a = 9.3157(4) Å b = 9.3157(4) Å c = 13.8689(13) Å β = 90 °
Volume (Å^3)	1203.57(15)
Z	1
Density (calculated) (g/m^3)	4.431
Absorption coefficient (mm^{-1})	12.850
F (000)	1396
Theta range for data collection	5.268 to 55.614 °
Index ranges	$-12 \le h \le 12$, $-12 \le k \le 12$, $-17 \le l \le 18$
Reflections collected	13224
Independent reflections	780 [$R_{(int)}$ = 0.0666]
Refinement method	Full-matrix least-squares on F^2
Goodness-of-fit on F_o^2	1.193
Final R indices [I > 2sigma(I)][a]	R_1 = 0.0520, wR_2 = 0.1049
R indices (all data)[a]	R_1 = 0.0548, wR_2 = 0.1069
Largest diff. peak and hole (e/Å^{-3})	1.95 and -2.47

[a] $R_1 = \Sigma||F_o| - |F_c||/\Sigma|F_o|$ and $wR_2 = [\Sigma w(F_o^2 - F_c^2)^2 / \Sigma wF_o^4]^{1/2}$ for $F_o^2 > 2\sigma(F_o^2)$

Table S2. Selected bond lengths [Å] and angles [deg] for $Sn_{11}(PS_4)_4I_{10}$.

$Sn_{11}(PS_4)_4I_{10}$			
P(1)-S(1)	2.040(4)	Sn(2)-S(1) #4	2.850(4)
P(1)-S(1) #1	2.040(4)	Sn(2)-S(1) #3	2.850(4)
P(1)-S(1) #3	2.040(4)	Sn(2)- I(1)	3.562(13)
P(1)-S(1) #5	2.040(4)	Sn(2)- I(1)	3.562(13)
Sn(1)-S(1)	2.876(5)	Sn(2)- I(1)	3.562(13)
Sn(1)-S(1)	2.876(5)	Sn(2)- I(1)	3.562(13)
Sn(1)-S(1) #1	2.999(50)	S(1) #7-P(1)-S(1) #1	110.5(2)
Sn(1)-S(1) #1	2.999(50)	S(1) #6-P(1)-S(1) #1	108.95(12)
Sn(1)- I(1)	2.904(3)	S(1) #7-P(1)-S(1) #5	108.95(12)
Sn(1)- I(2)	3.624(25)	S(1)-P(1)-S(1) #6	108.95(12)
Sn(2)-S(1) #1	2.850(4)	S(1)-P(1)-S(1) #5	110.5(2)
Sn(2)-S(1) #2	2.850(4)	S(1)-P(1)-S(1) #1	108.95(12)

Symmetry transformations used to generate equivalent atoms: #1 1/2+*x*, 1/2-*y*, 3/2-*z*; #2 1/2-*x*, 1/2-*y*, -1/2+*z*; #3 1/2-*x*, -1/2+*y*, 3/2-*z*; #4 1/2+*x*, -1/2+*y*, -1/2+*z*; #5 -x, 1-y, *z*; #6 1/2-*x*, -1/2+*y*, 3/2-*z*;

Table S3. Atomic coordinates, equivalent isotropic displacement parameter and bond valence sum (BVS) for $Sn_{11}(PS_4)_4I_{10}$.

Atom	Wyck.	Site symmetry	*x*	*y*	*z*	U_{eq}[a]	S.O.F	BVS
Sn(1)	8*i*	*m*	3501(2)	3501(2)	7191(2)	92.2(10)	1	1.67
Sn(2)	4*c*	222	0	5000	5000	93.9(18)	0.75	1.66
P(1)	4*d*	$\bar{4}$	0	5000	7500	39.8(18)	1	5.05
S(1)	16*j*	1	930(5)	3460(5)	8338(3)	44.2(10)	1	2.08
I(1)	8*i*	*m*	1875.3(14)	1875.3(14)	5777.0(11)	50.3(5)	1	0.87
I(2)	2*a*	$\bar{4}2m$	5000	5000	5000	54.9(9)	1	0.38

[a] U_{eq} is defined as one-third of the trace of the orthogonalized U_{ij} tensor.

Table S4. The LIDT of $Sn_{11}(PS_4)_4I_{10}$.

Compounds	Damage energy (mJ)	Spot diameter (cm^2)	τ_p (ns)	LIDT [$MW \cdot cm^{-2}$]
SPSI	10.9	0.096	10	11.3
AGS	3.3	0.096	10	3.4

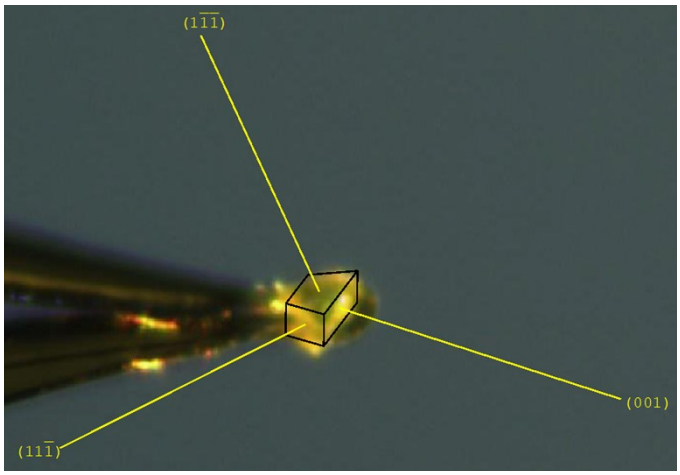

Figure S1. The index crystal faces of $Sn_{11}(PS_4)_4I_{10}$.

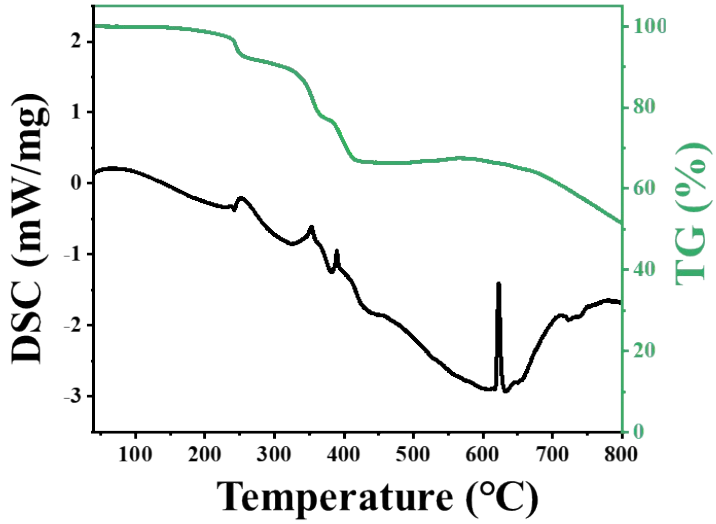

Figure S2. The TG-DSC curve of $Sn_{11}(PS_4)_4I_{10}$. It can be seen that there are endothermic peaks at 300 °C on the DSC curves for $Sn_{11}(PS_4)_4 I_{10}$, along with weight loss on the TG curves.

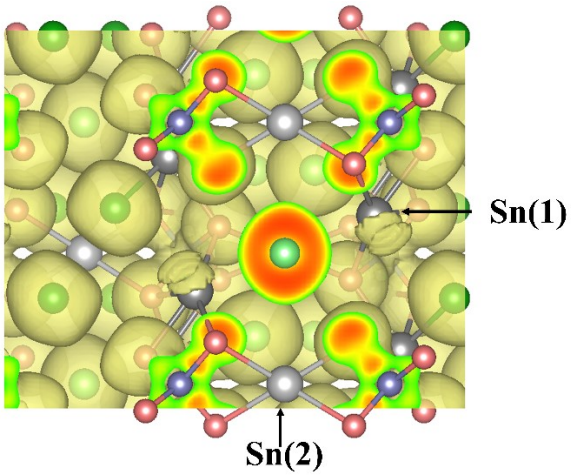

Figure S3. The electron distribution of Sn(1) and Sn(2).

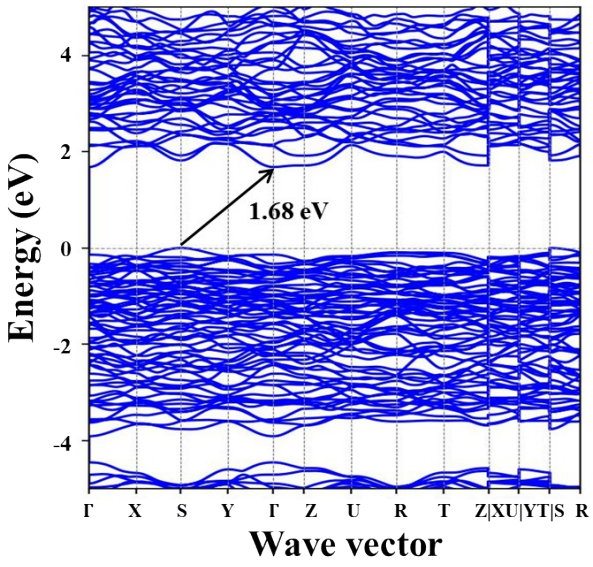

Figure S4. The PBE calculated band structure of $Sn_{11}(PS_4)_4I_{10}$.

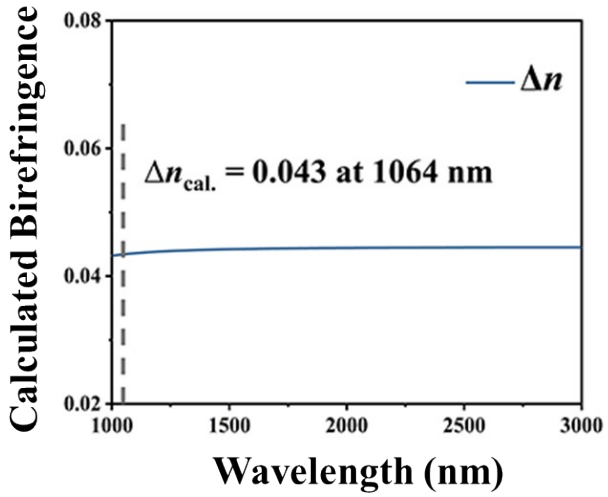

Figure S5. The calculated birefringence of $Sn_{11}(PS_4)_4I_{10}$.

References

1 SAINT, *version 7.60A*, Bruker Analytical X-ray Instruments, Inc., Madison, WI, 2013.
2 SHELXTL, *version 6.1*., Bruker Analytical X-ray Instruments, Inc., Madison, WI, 2013.
3 P. Kubelka, F. Munk, An article on optics of paint layers, *Tech. Phys.*, 1931, **12**, 593−609.
4 S. K. Kurtz, T. T. Perry, A powder technique for the evaluation of nonlinear optical materials, *J. Appl. Phys.*, 1968, **39**, 3798–3813.
5 Y. H. Hu, X. Xu, R. X. Wang, J. Y. Han, S. S. Zhang, S. H. Zhang, J. Y. Guo, Wu, L. M. Wu, L. Chen, $[Sn_3OF]PO_4$ vs $[Sn_3F_3]PO_4$: Enhancing birefringence through breaking R3 symmetry and realigning lone pairs, *Inorg. Chem. Front.*, 2024, **11**, 5648−5656.
6 P. Hohenberg, W. Kohn, Density functional theory (DFT). *Phys. Rev.*, 1964, **136**, B864-B871.
7 W. Kohn, L. Sham, Self-consistent equations including exchange and correlation effects, *Phys. Rev.*, 1965, **140**, A1133-A1138.
8 P. E. Blöchl, Projector Augmented-Wave Method, *Phys. Rev. B*, 1994, **50**, 17953–17979.
9 M. Gajdoš, K. Hummer, G. Kresse, J. Furthmüller, F. Bechstedt, Linear optical properties in the projector-augmented wave methodology, *Phys. Rev. B*, 2006, **73**, 045112.
10 X. Gonze, B. Amadon, G. Antonius, F. Arnardi, L. Baguet, J. M. Beuken, J. Bieder, F. Bottin, J. Bouchet, E. Bousquet, N. Brouwer, F. Bruneval, G. Brunin, T. Cavignac, J. B. Charraud, W. Chen, M. Côté, S. Cottenier, J.; Denier, G. Geneste, P. Ghosez, M. Giantomassi, Y. Gillet, O. Gingras, D. R. Hamann, G. Hautier, X. He, N. Helbig, N. Holzwarth, Y. Jia, F. Jollet, W. Lafargue-Dit-Hauret, K. Lejaeghere, M. A. L. Marques, A. Martin, C. Martins, H. P. C. Miranda, F. Naccarato, K. Persson, G. Petretto, V. Planes, Y. Pouillon, S. Prokhorenko, F. Ricci, G. M. Rignanese, A. H. Romero, M. M. Schmitt, M. Torrent, M. J. Van Setten, B. Van Troeye, M. J. Verstraete, G. Zérah, J. W. Zwanziger, The abinit project: Impact, environment and recent developments, *Comput. Phys. Commun.*, 2020, **248**, 107042.
11 M. Veithen, X. Gonze, Ph. Ghosez, Nonlinear optical susceptibilities, raman efficiencies, and electro-optic tensors from first-principles density functional perturbation theory, *Phys. Rev. B*, 2005, **71**, 125107.